JOURNAL OF MATERIALS SCIENCE **34** (1999) 735–747

Structure and properties of rapidly solidified Al rich Al-Mn-Si alloys

Part I *Melt spun ribbons*

D. M. J. WILKES*, H. JONES
Department of Engineering Materials, University of Sheffield, Sheffield S1 3JD, UK
E-mail: k.a.burton@sheffield.ac.uk

The evolution of microstructure as-spun and during subsequent heat treatment at 200 to 500 °C for up to 1000 h has been studied for Al-6.3 Mn-3.3 Si, Al-8.3 Mn-3.7 Si and Al-14.5 Mn-5.8 Si (wt %) alloys, containing 17, 26 and 48 vol % αAlMnSi at equilibrium respectively. Microstructure as-spun ranged from primary icosahedral phase nucleating radial cellular αAl arrays to less regular duplex arrays of αAl and αAlMnSi with decreasing alloy content and decreased section thickness or reduced distance from the chill surface. Heat treatment in the range 200 to 500 °C transformed any icosahedral phase present to αAlMnSi along with spheroidization and coarsening/coalescence of αAlMnSi, to produce isolated spheroids when volume fraction f was lower and very stable interlinked chains at higher f. Measured coarsening rates of αAlMnSi were a factor of 10 below predictions of LSW theory at lower f but were within a factor of 2 of prediction at highest f. Hardness was governed by a combination of Hall-Petch and matrix solid solution hardening as-spun supplanted by particle-radius dependent Orowan combined with matrix Hall-Petch hardening for the evolution of hardness during prior long term heat treatment at 425 °C.

1. Introduction

The effectiveness of a high volume fraction of nano-sized silicide dispersoid for conferring strength and stability on aluminium matrices at elevated temperature is exemplified by the state of the art rapidly solidified 8009 Al-Fe-V-Si alloy developed by Allied Signal [1, 2]. This material exhibits remarkable microstructural stability during extended treatments at temperatures as high as 0.75 T_m (425 °C) although transformation of the spheroidal $\alpha Al_{13}(Fe, V)_3Si$ strengthening dispersoid to embrittling needles of equilibrium $Al_{13}Fe_4$ starts to occur at 480 to 600 °C (0.81 to 0.94 T_m) [3–5]. The corresponding $\alpha Al_{15}Mn_3Si_2$ dispersoid in the Al-Mn-Si system is a stable phase and previous work on consolidated Al-Mn-Si alloy atomized powder particulate has yielded promising results as an alternative to systems based on Al-Fe-Si [6–16].

The present work formed part of a programme to explore the potential of rapidly solidified Al-Mn-Si alloys as a basis for achieving high strength along with high thermal stability both as a monolithic material and as matrix material for ceramic reinforcement. Some of the results obtained were reported earlier [17, 18]. The second of these two papers reported on the effect of variable silicon content over the range 2.7 to 9.8 wt % Si on the structure and stability of Al-7.5 wt % Mn melt-spun ribbon. The present paper features the corresponding results for three melt-spun alloys designed to give a fixed 0.8 wt % Si in the matrix and 17, 26 and 48 vol % $\alpha Al_{15}Mn_3Si_2$ dispersoid at equilibrium. Part II of this paper** will report the structure and performance of an Al-Mn-Si alloy consolidated from atomized prealloyed powder with and without an addition of silicon carbide.

2. Experimental

Alloys of composition Al-6.3 Mn-3.3 Si, Al-8.9 Mn-4.0 Si and Al-13.8 Mn-4.2 Si (wt %), designated AMS 63, 94 and 135 respectively, were made first as ingots of dimensions 16 × 50 × 150 mm by vacuum induction melting 99.999% Al with Al-Mn and Al-Si master alloys and chill casting under argon. Samples of 8009 Al-Fe-V-Si alloy were obtained as 1 mm thick hot rolled sheet from British Aerospace at Warton, for comparison. 10 g charges were remelted in silica nozzles and chill block melt spun on copper at a wheel speed of 21 m/s into rapidly solidified ribbon of thickness typically between 30 and 40 μm and width ~2 mm to give the ribbon compositions indicated in Table I. Heat treatments were carried out at 200 to 600 °C for 2 to 1000 h on samples wrapped in aluminium foil in silica ampoules that had been evacuated to 10^{-5} torr and refilled with 250 torr of argon prior to sealing. Samples for optical metallography were edge mounted in cold-setting resin for grinding and polishing, finishing with

* *Present Address*: Structural Materials Centre, DERA Farnborough, GU14 0LX, UK.
** This issue, pp. 749–761.

TABLE I Alloy compositions (wt %, balance aluminium) with their designations and calculated equilibrium volume fractions of silicide

Designation	AMS 63	AMS 94	AMS 135	8009
Composition	6.3 Mn, 3.3 Si	8.3 Mn, 3.7 Si	14.5 Mn, 5.8 Si	8.1 Fe, 1.2 V, 2.0 Si
Vol % silicide	17	26	48	27

a 0.25 μm aqueous silica suspension before etching in Murakami's reagent. X-ray diffraction used CoKα radiation on pieces of ribbon stuck onto glass slides by means of UHU glue dissolved in acetone. Thinning for TEM was achieved by electropolishing in a solution of 25% nitric acid in methanol at below $-30\,^{\circ}$C, or by ion beam milling with liquid nitrogen cooling. Dispersoid particle sizes in samples were determined both directly via TEM and in directly from X-ray peak breadth measurements. The TEM measurements sampled at least 300 particles measured for each condition. X-ray peak breadths at half maximum intensity were measured for up to 5 low angle peaks and corrected for α_1/α_2 splitting and instrumental broadening by reference to a pure quartz standard with a very large grain size. Microhardness testing used a Knoop indenter with a load of 25 g applied for 12 seconds on edge mounted samples. Reported results are the average of at least 15 indentations per condition.

3. Results

3.1. Microstructure as-spun

Etched microsections showed both optically featureless (zone A) areas adjacent to the chill surface and areas (zone B) that responded to etching, which revealed dispersoids of up to 2 μm in size, many with a five-fold star morphology (Fig. 1) towards the free surfaces of the AMS 135 and 94 ribbons. X-ray diffraction showed peaks corresponding in position to αAl and αAlMnSi [19] or i-AlMn(Si) [20–22]. Fig. 2 shows X-ray traces from the critical range of 2θ for the as-spun condition. The peaks labelled M11, M12 and M13 for AMS 63 and 94 match well in position and relative intensity with 433, 600 and 611 from αAlMnSi. The relative intensities of the corresponding three peaks, however, do not match well with αAlMnSi for AMS 135. Peak M12 has become weaker and the peaks I3 and I4 are a good match in position and relative intensity with 100000 and 110000 from i-AlMn(Si), indicating dominance of the icosahedral (i-) phase with a smaller contribution from αAlMnSi.

TEM of AMS 135 showed rosette-like regions 1 to 2 μm across with dispersoid particles at their centre (Fig. 3a–e). These central particles had flower-like (Fig. 3a, e) or spheroidal (Fig. 3c) morphology with diffraction patterns (Fig. 3b, d) corresponding to the i-phase indicated by XRD. Cellular αAl with intercellular second phase radiated outwards from these particles. Samples thinned from the chill or free sides showed higher volume fraction of the i-phase particles towards the free surface and an increased fraction of cellular αAl towards the chill surface, where many areas contained no i-phase or other particle at their centre, confirming the findings of optical metallography. The corresponding AMS 94 samples showed some i-phase areas similar to Fig. 3a–e but mainly comprised discrete globular particles, 60 to 90 μm in size, identified as αAlMnSi in the αAl matrix (Fig. 4a, b). AMS 63 samples were predominantly microcellular αAl with discrete or continuous intercellular second phase (Fig. 5a, b). The presence of the i-phase was not detected, with diffraction from the intercellular phase being consistent with αAlMnSi.

3.2. Effect of heat treatment

Heat treatment of AMS 135 for 2 h at increasing temperatures between 200 and 500 $^{\circ}$C resulted in a systematic

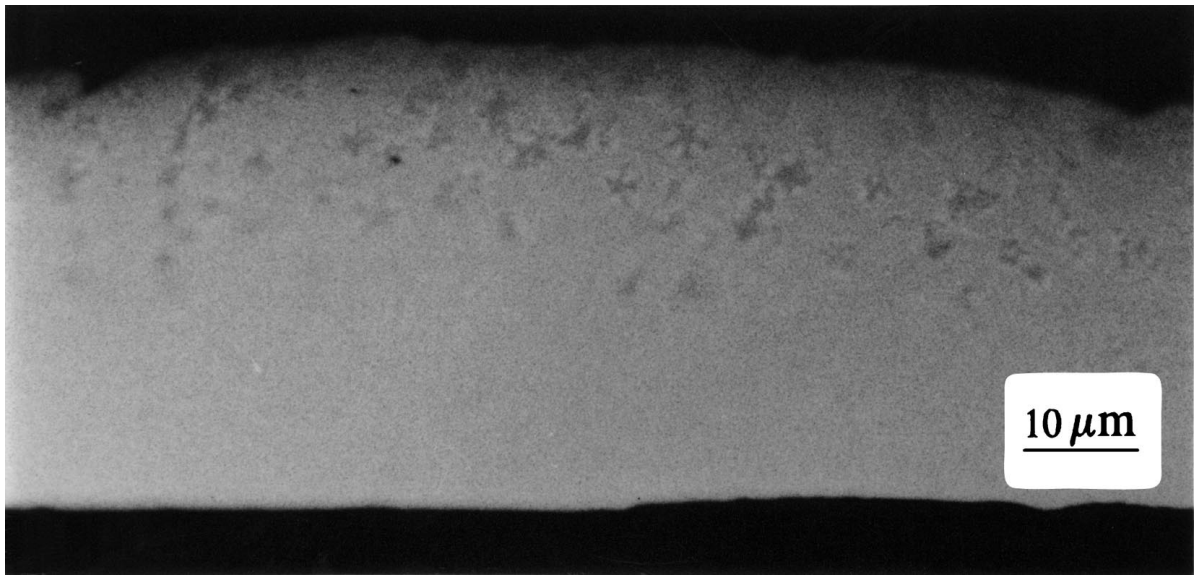

Figure 1 Optical micrograph of etched microsection of as-spun AMS 135 showing particles with five-fold star morphology near the free surface.

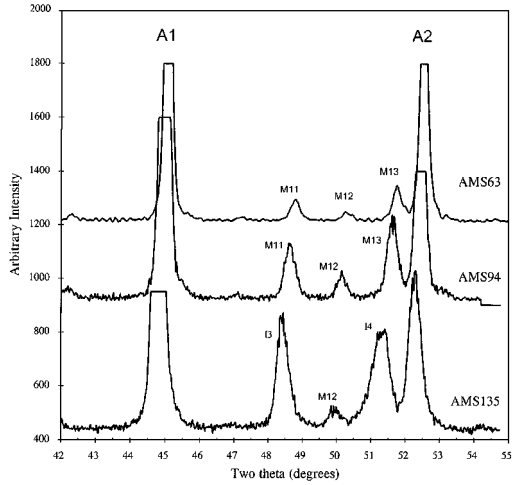

Figure 2 X-ray traces from as-spun AMS 63, 94 and 135. Key to phases:

Phase	αAl		αAlMnSi			i-AlMn(Si)	
Peak designation	A1	A2	M11	M12	M13	I3	I4
Index hkl	111	200	433	600	611	100	80
Relative intensity	100	40	90	60	100	100000	110000
2θ in degrees	45.1	52.5	48.6	50.1	51.6	48.7	51.4

Data for αAl and αAlMnSi from powder diffraction file cards 4-0787 and 6-0669.
Data for i-AlMn(Si) from Bancel et al. [20]
2θ values are for CoKα radiation, $\lambda = 0.17902$ nm

change in the relative intensities of the peaks at 48.6 and 51.6 degrees 2θ from dominance of the former (characteristic of the i-phase) to dominance of the latter (characteristic of αAlMnSi) as shown in Fig. 6a. After 2 h at 500 °C the relative intensities and positions of the second phase peaks M7 to M15 in Fig. 6a are a good match with αAlMnSi. Fig. 6b shows that similar treatment of AMS 94 gave a sharpening and intensification of the second phase peaks for 300 °C and above, but the relative intensities of the prominent peaks did not change. Treatment at 500 °C, however, gave an unusual increase in the intensity of the 45.5°2θ (M14) peaks. Correspondingly for AMS 63 relative intensities remained the same as for the as-spun conditions with some increase in absolute intensities after 2 h at 500 °C.

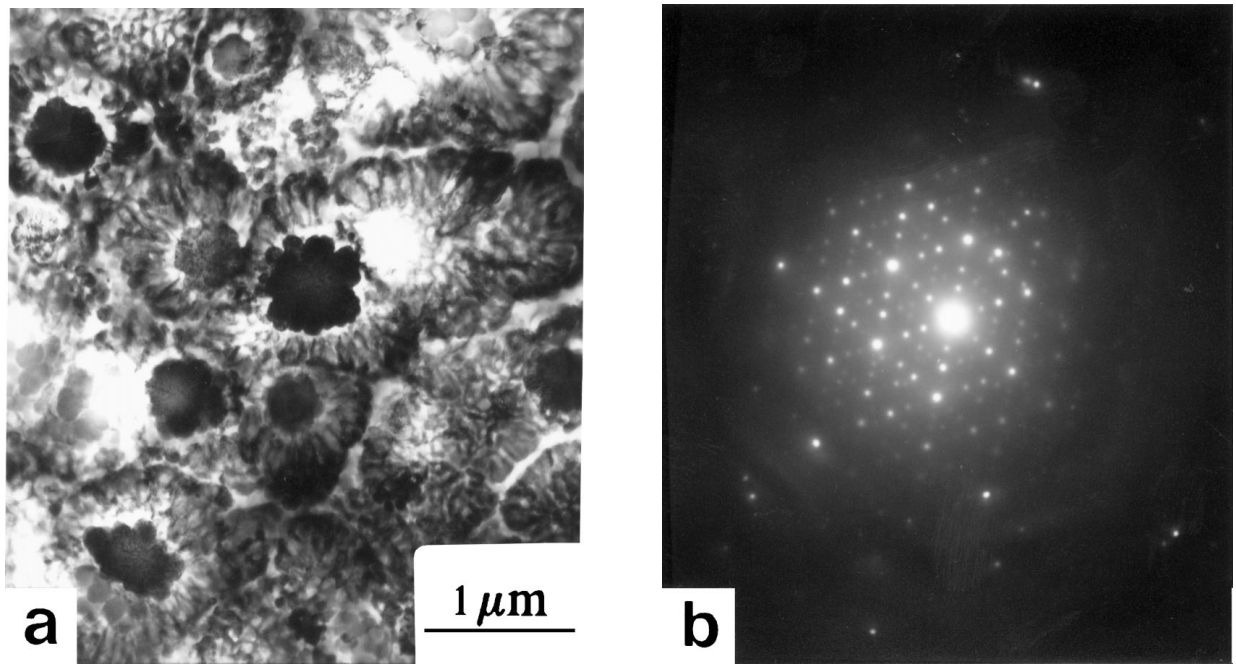

Figure 3 TEM micrographs of as-spun AMS 135 showing flower-like (a, e) and spheroidal (c) i-phase particles in a cellular αAl matrix, with 3-fold (b) and 2-fold (d) diffraction patterns from the i-phase. (*Continued*).

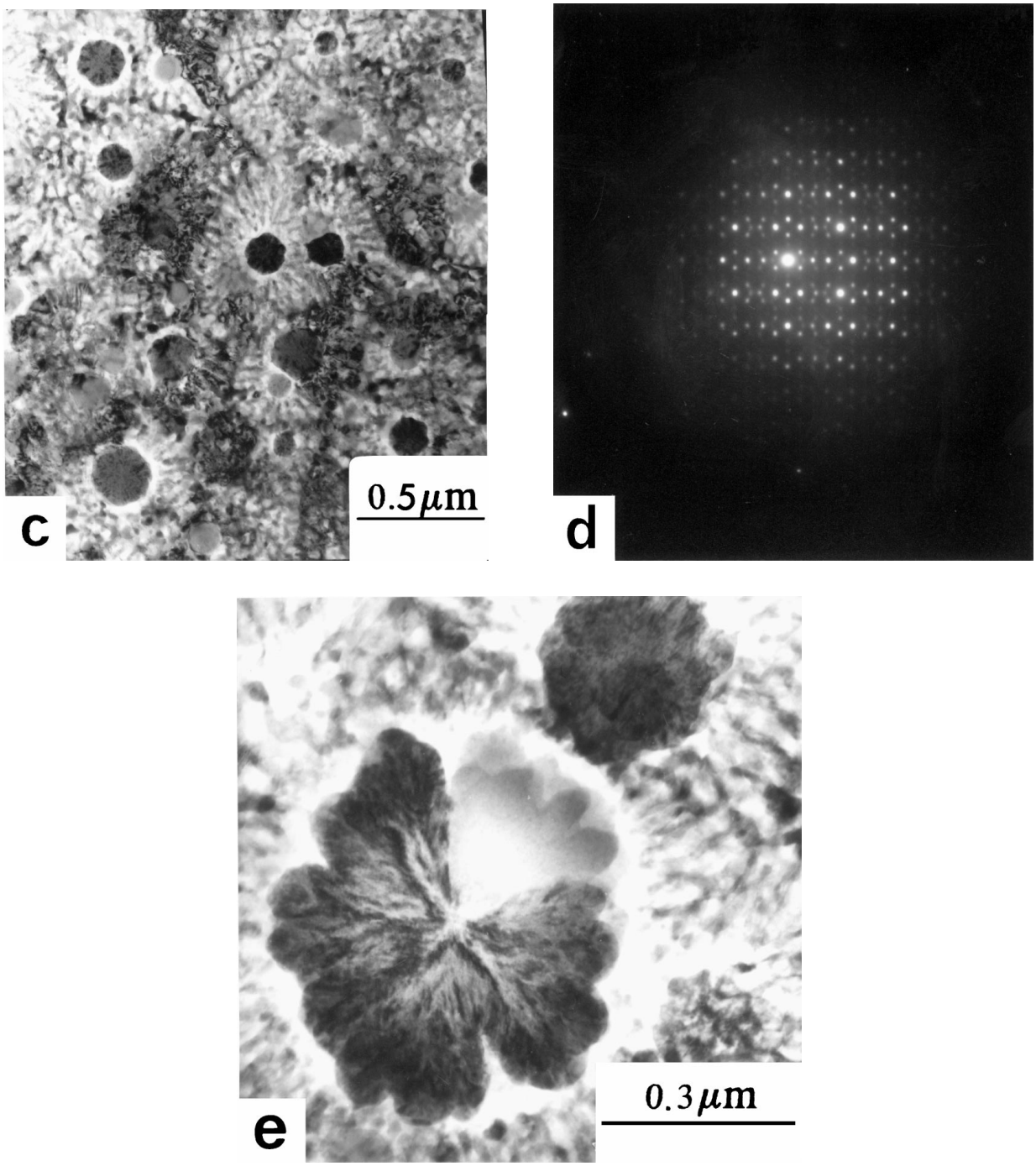

Figure 3 (*Continued*).

TEM of AMS 135 after 2 h at 200 °C showed a high volume fraction of clusters of small particles with diffraction patterns corresponding to the i-phase but with quite different morphology from the i-phase rosettes in the as-spun ribbon (Fig. 7a–d). Treatment for 2 h at 425 °C in contrast gave a high volume fraction of spherical αAlMnSi particles 100 to 200 nm in size, mainly situated on cell or subgrain boundaries (Fig. 8a). Little coarsening of these particles was evident after 100 h at 425 °C (Fig. 8b), though some instances of the initial stages of coalescence of neighbouring particles were identified. No significant further increase in size of most of the αAlMnSi particles or the αAl subgrains was apparent after 1000 h at 425 °C (Fig. 8c). Some particle clusters had almost fully coalesced into single larger particles, however, after this prolonged treatment. AMS 94 after 2 h at 425 °C had a similar microstructure to the as-spun material but with spheroidization of cellular arrays surrounding any remnant i-phases (Fig. 9a). AMS 63 also showed a high volume fraction of spheroidal particles after 2 h at 425 °C (Fig. 9b). In some areas small plate-like or angular particles were also visible. Diffraction patterns identified the larger spheroidal particles as αAlMnSi and the other particles were not evident in the sample treated for 100 h at 425 °C. This sample (Fig. 10a) showed a homogenous distribution of fine αAlMnSi within αAl grains together with particles situated at triple points which had grown considerably. 1000 h at 425 °C produced some coarsening of particles within the αAl grains, slight elongation

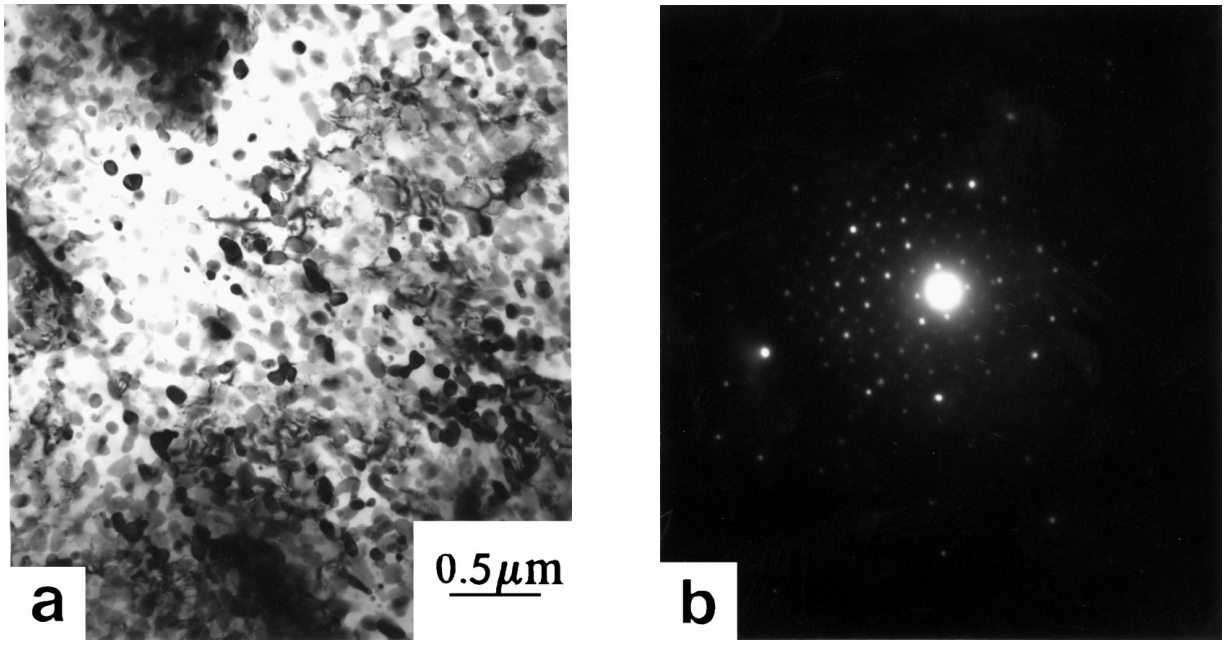

Figure 4 TEM micrographs of as-spun AMS 94 showing (a) fine globular αAlMnSi in the αAl matrix and (b) αAlMnSi diffraction pattern. Some i-phase areas similar to Fig. 3a–e were also present.

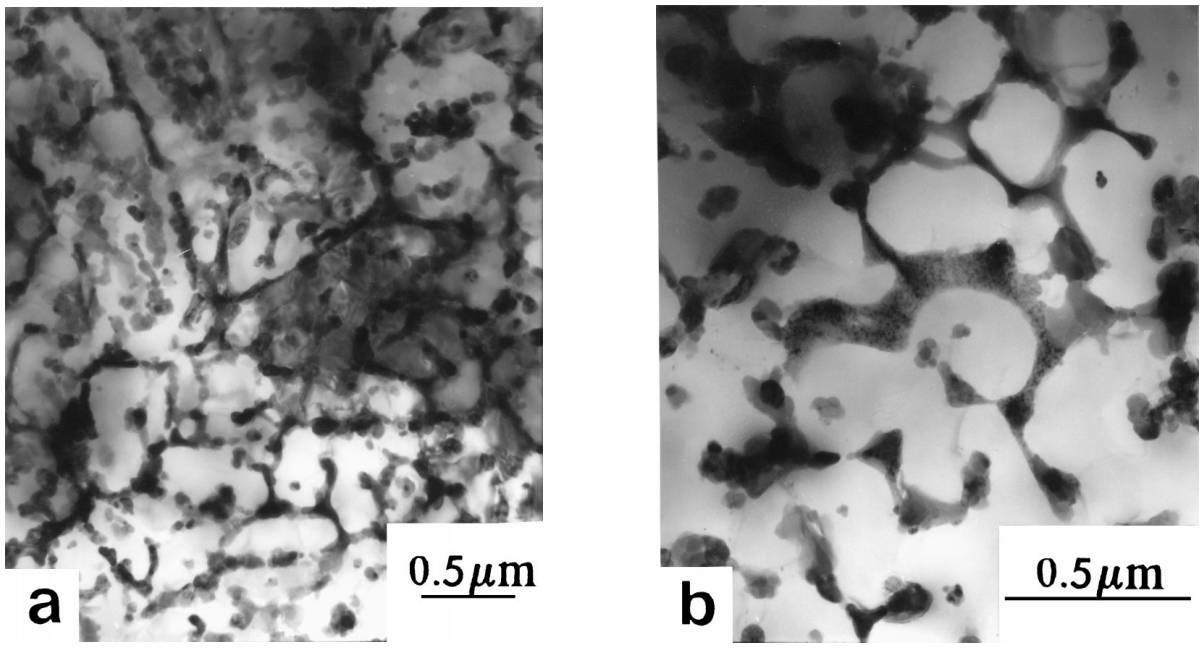

Figure 5 TEM micrographs of as-spun AMS 63 showing (a) semicontinuous and discrete and (b) continuous intercellular αAlMnSi in the αAl matrix.

in the boundary plane of particles growing on αAl grain faces and significant further growth of triple point particles (Fig. 10b).

Table II shows mean radius r of αAlMnSi particles versus time from 5 to 1000 h at 425 °C. Most of these results were obtained by X-ray diffraction with measurements by TEM included for comparison where available to confirm the validity of the XRD results. The results for AMS 135 show no significant change in r over this time interval, while AMS 94 shows some

TABLE II Mean radius $\bar{r}$ in nm of αAlMnSi particles in melt spun AMS alloys versus duration t of prior heat treatment at 425 °C

t,h	O	2	5	15	50	100	200	500	1000
AMS 135	—	—	76 ± 11	69 ± 10	72 ± 11	73 ± 11 $^{*}70 \pm 4$	72 ± 11	73 ± 11	74 ± 11 $^{*}77 \pm 2$
AMS 94	—	—	54 ± 8	67 ± 10	—	62 ± 9	67 ± 10	81 ± 12	76 ± 11
AMS 63	22 ± 3	36 ± 5	34 ± 5	45 ± 7	53 ± 8 $^{*}51 \pm 1$	54 ± 8 $^{*}47 \pm 1$	60 ± 9	69 ± 10	83 ± 12 $^{*}85 \pm 3$

Measurements made from X-ray peak breadth, verified * by TEM

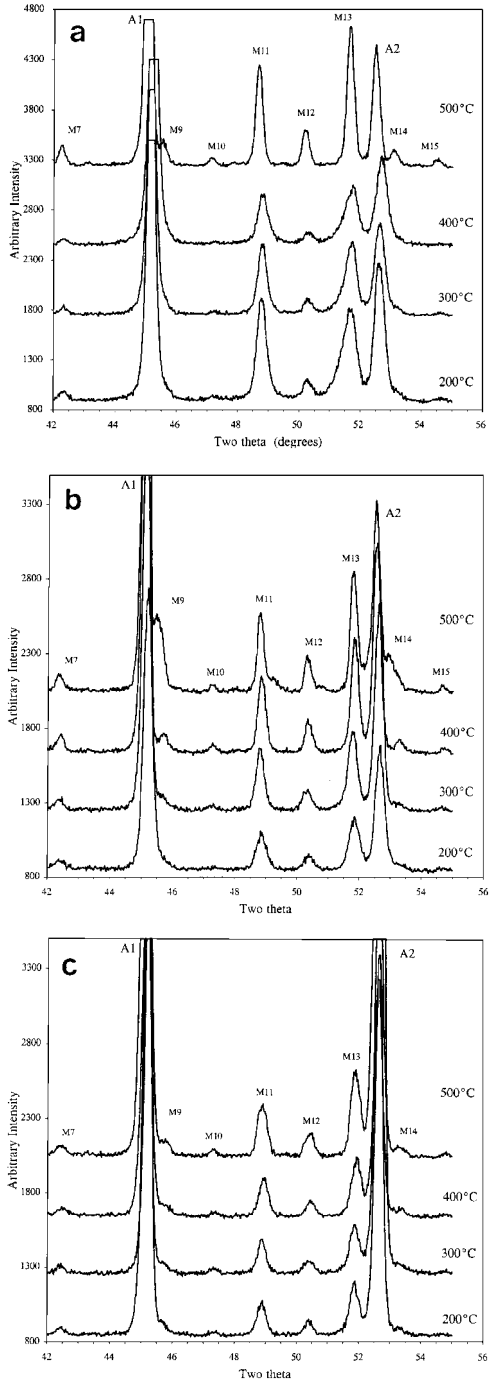

Figure 6 X-ray traces from AMS 135, 94 and 63 respectively after 2 h at 200, 300, 400 and 500 °C. Key to phases as in Fig. 2 plus additional data for αAlMnSi as follows:

Peak designation	M7	M9	M10	M14	M15
Index hkl	510	521	440	620	541
Relative intensity	50	50	10	40	10
2θ in degrees	42.1	45.5	47.0	53.0	54.5

change and AMS 63 shows a significant change. Example of size distributions of particle radii from the TEM measurements are shown in Fig. 11a, b.

3.3. Microhardness measurements

Knoop microhardness HK versus temperature of 2 h prior isochronal treatment is shown in Fig. 12a with results for melt spun 8009 alloy for comparison. AMS 135 shows a notable increase in HK on treatment at 200 °C compared with as-spun material and after treatment at 160 °C, with treatment at 300, 400 and 500 °C producing successively lower values. Any such hardness increase was small for AMS 94 and AMS 63, which showed a gradual decrease in HK on treatment at 200 °C and above similar to that shown for 8009 alloy. Corresponding results for microhardness HK versus time of prior treatment at 425 °C are shown in Fig. 12b. All four alloys show a substantial decrease in HK in the initial 5 h at 425 °C followed by more gradual decreases between 5 and 1000 h.

4. Discussion

4.1. Formation of microstructure as-spun

The zoned microstructures shown by optical microscopy are typical of rapidly solidified alloy samples based on aluminium with significant additions of transition metals [23–25]. The optically featureless zone A microstructure is formed under conditions of large prior undercooling which allows rapid advance of the solidification front during recalescence. The significantly coarser zone B structure forms with a slower rate of advance sustained by external heat extraction in the absence of significant prior undercooling or following its dissipation in forming zone A [24, 25]. More concentrated alloys exhibit distributions of primary intermetallics ~0.1 to a few μm in size surrounded by cellular αAl arrays with intercellular intermetallics, as in Fig. 3 for AMS 135. The primary and secondary intermetallics need not be the same phase and can feature equilibrium and/or nonequilibrium phases (or their combinations) and the αAl matrix can exhibit extension of solid solubility, the extent of which depends on the local solidification conditions. The formation of i-AlMn(Si) in competition with equilibrium Al_6Mn or αAlMnSi is well documented for a range of alloying contents in Al-Mn(-Si) alloys under rapid solidification conditions [26–31]. Our results indicate that it is on the point of disappearing as a primary phase in our melt spun AMS 94, with the consequence that the radial cellular αAl arrays surrounding primary i-AlMnSi in AMS 135 are replaced in AMS 94 by the less well-defined duplex structure of Fig. 4 giving way to the cellular αAl structure in AMS 63 shown in Fig. 5. The highest incidence of primary i-AlMnSi particles towards the free side of melt spun AMS 135 (evident to a lesser extent in AMS 94) and in thicker sections of ribbon is consistent with the expectation that solidification occurs at relatively lower undercoolings there and that the higher undercoolings prevailing near chill surfaces and in thinner sections tend to suppress the formation of primary intermetallics.

The progressive shift of the αAl reflections in Fig. 2 to lower 2θ values with increase in alloying from AMS 63 to 135 is indicative of increasing αAl lattice parameter and (since both Mn and Si reduce the lattice parameter of αAl) less extension of solid solubility. Such an increase of αAl lattice parameter with increase in alloy content under conditions where the i-phase formed

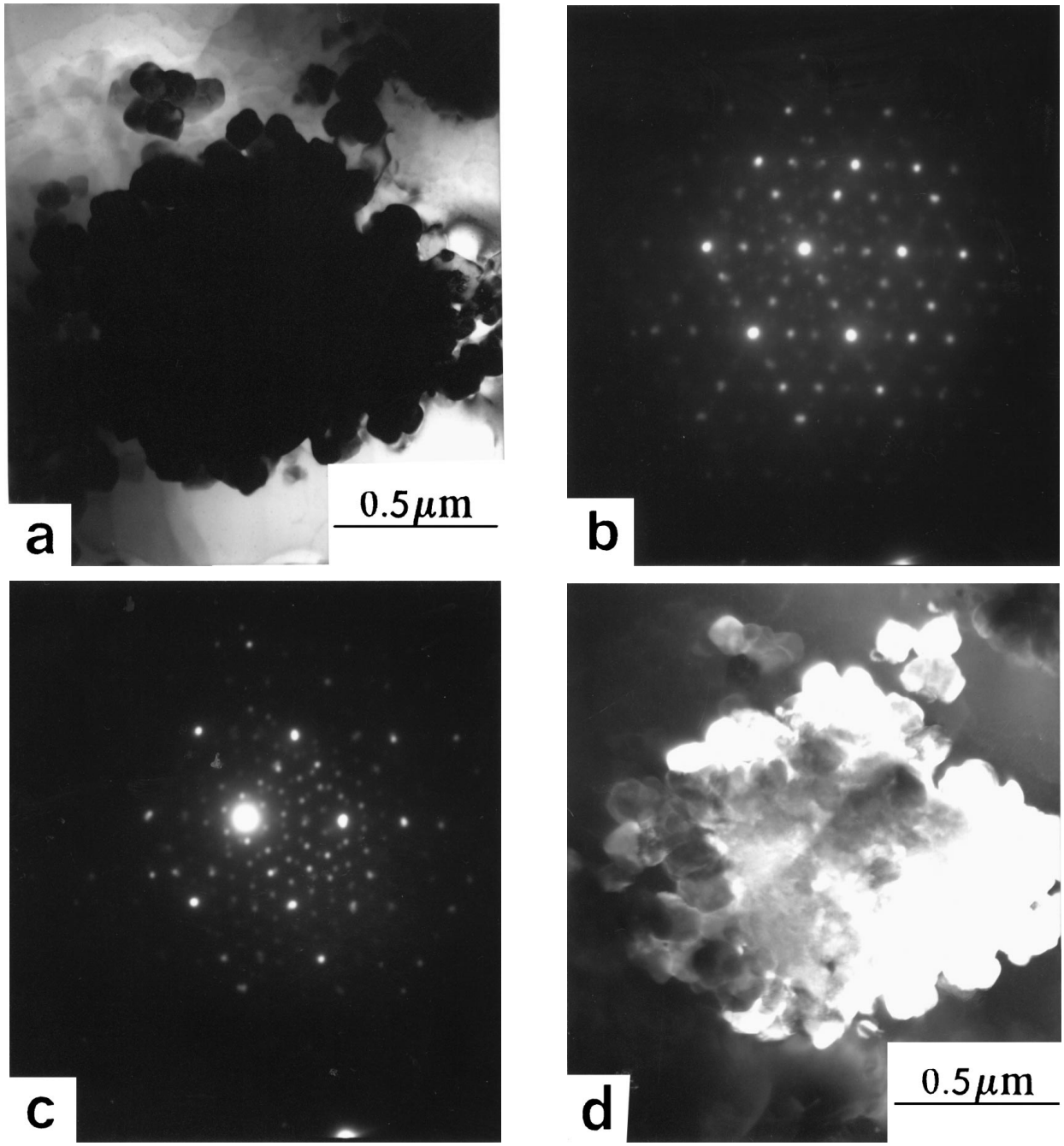

Figure 7 TEM micrographs of a second phase cluster in AMS 135 after 2 h at 200 °C (a) brightfield (b) i-phase DP from centre of cluster (c) cubic αAlMnSi DP from edge of cluster, and (d) dark field from $\overline{2}\,\overline{3}1$ αAlMnSi showing location of αAlMnSi.

was also noted by Schaefer *et al.* [26] for melt spun Al-Mn alloys. Bendersky and Ridder [32] obtained experimentally for the i-phase grain size Λ in Al-14 at % Mn alloy atomized droplets:

$$\Lambda = a\dot{T}^{-1.7} \quad (1)$$

where $\dot{T}$ is cooling rate and $a = 7$ m(K/s)$^{1.7}$. The cell size ~300 nm of Fig. 3 would correspond to an operative cooling rate $\sim 2 \times 10^4$ K/s, below the lower end of the range expected [33] for melt-spinning of ribbon 30 to 40 μm in thickness. The corresponding relationship for αAl cell size in representative Al alloys gives [34]:

$$\lambda = b\dot{T}^{-1.3} \quad (2)$$

with $b = 50$ μm (K/s)$^{1/3}$ which for the αAl cell size ~0.3 μm in Fig. 5 gives $\dot{T} \sim 5 \times 10^6$ K/s, towards the upper end of the range expected.

4.2. Transformations on heat treatment

The transformation of nonequilibrium i-phase to equilibrium intermetallics has been studied both for Al-Mn alloys where the product, directly or eventually, is Al_6Mn [27, 29–31, 35–44] and for Al-Mn-Si alloys where the result is αAlMnSi [30, 44–52]. Onset temperatures as low as ~300 °C [37, 40–43] have been determined for i-phase to transform to Al_6Mn in Al-Mn alloys with the transformation complete within 1 h at 400 °C [25, 37] while transformation of i-phase to αAlMnSi or other products starts at ~400 °C in

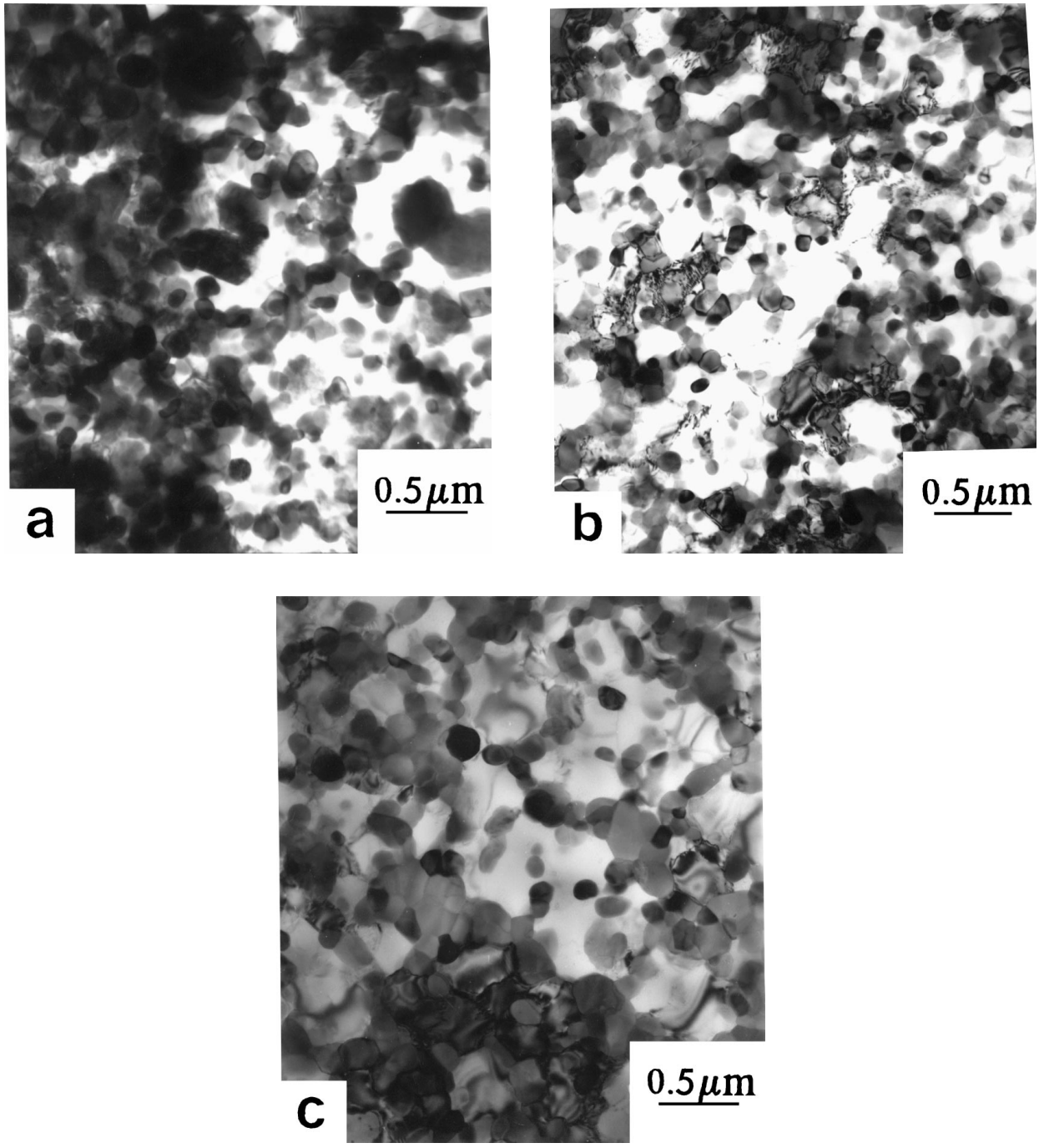

Figure 8 TEM micrographs of AMS 135 after (a) 2 (b) 100 and (c) 1000 h at 425 °C.

Al-Mn-Si alloys [30, 46, 47]. The observation of what appears to be the beginnings of transformation in AMS 135 at 200 °C in Fig. 7a–d is at odds with these previous observations, though the location of the product phase at the interface between the i-phase and the αAl matrix does accord with earlier reports [37, 50]. One possibility is that the close similarities between the local structure of the i-phase and αAlMnSi in Al-Mn-Si [53, 54] could reduce energy barriers compared to the i-phase to Al_6Mn transformation in Al-Mn alloys. A further possibility is that partial transformation to α-silicide had begun at the periphery of i-phase particles even in as-spun material, as was found by Park *et al.* [55] for Al-Fe-V-Si. The diffraction patterns in Fig. 7a–d suggest that αAlMnSi forms with its [111] zone parallel to the 3-fold zone axis of the i-phase. Hansen *et al.* [50] also found a relationship of this kind as well as [530] αAlMnSi//5-fold axis of i-phase and [100] αAlMnSi//2-fold axis of i-phase.

4.3. Spheroidization and coarsening or coalescence of αAlMnSi in prolonged heat treatment

Both X-ray diffraction and TEM confirmed that all of any i-phase had transformed to αAlMnSi within 2 h at 425 °C. At this stage AMS 135 contained chains or isolated spheroids of αAlMnSi (Fig. 8a) with only some larger clusters remaining and after 1000 h this microstructure was essentially still intact (Fig. 8c) with no detectable coarsening (Table II). The initial distribution in αAlMnSi areas of AMS 94 was not dissimilar and

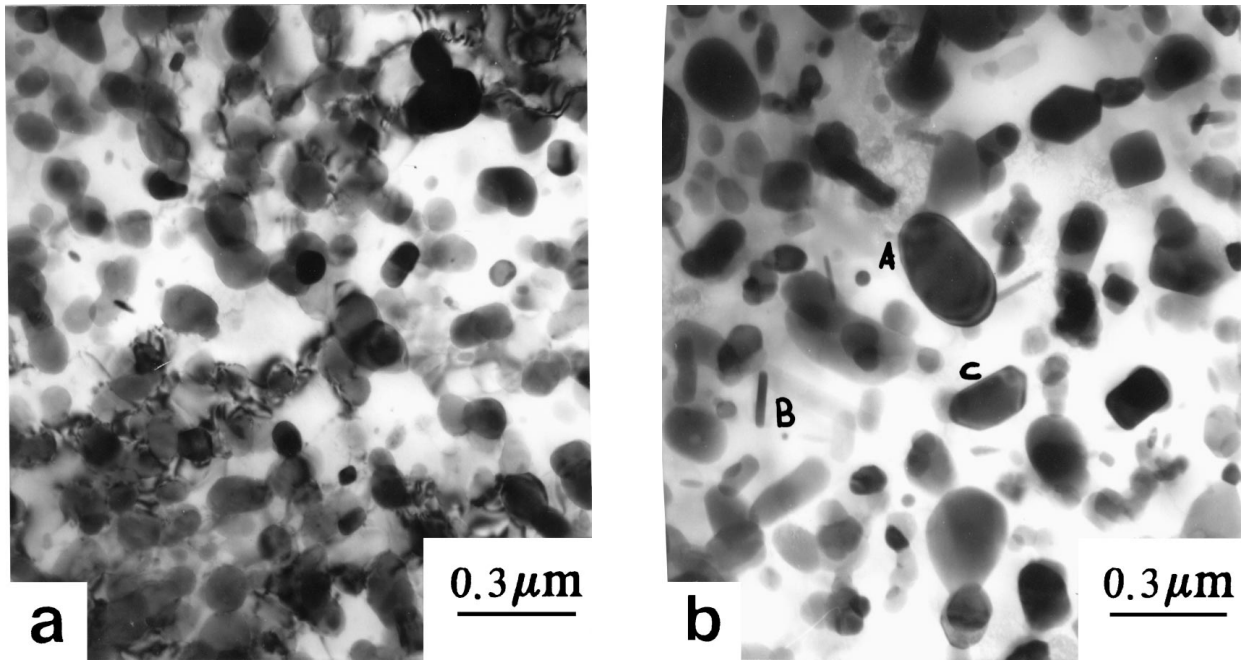

Figure 9 TEM micrographs of (a) AMS 94 and (b) AMS 63 after 2 h at 425 °C showing spheroidal αAlMnSi particles (A) along with plates (B) and angular particles/tilted plates (C).

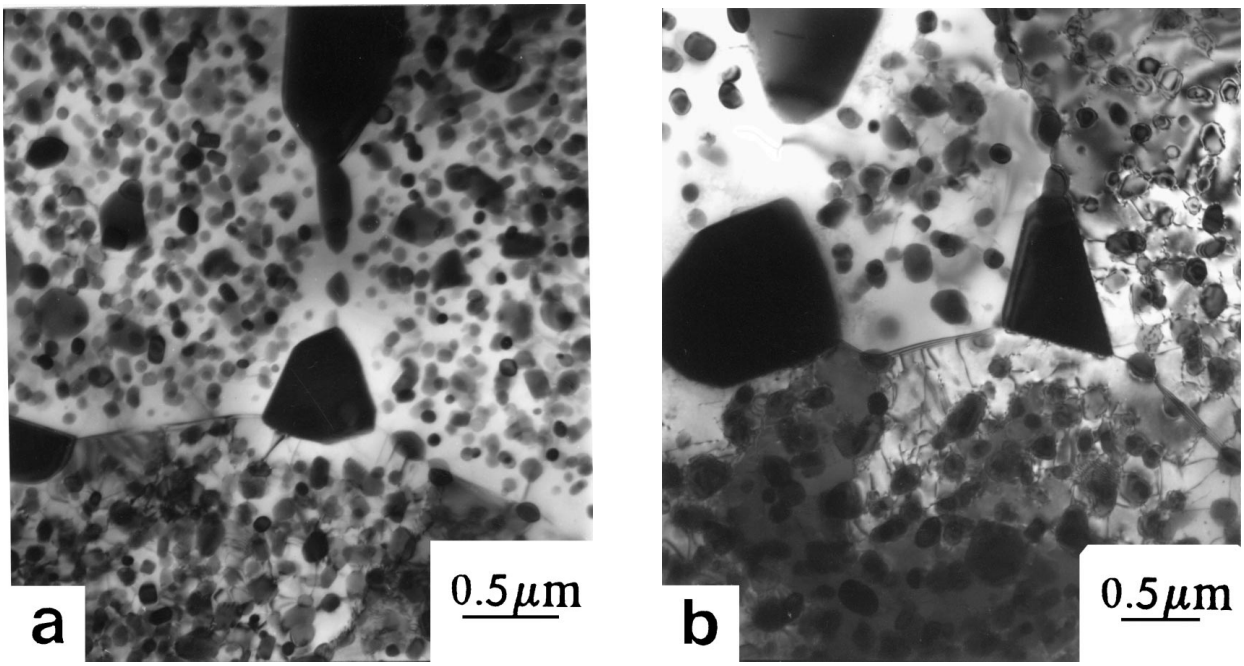

Figure 10 TEM micrographs of AMS 63 after (a) 100 and (b) 1000 h at 425 °C showing large particles at triple points.

again there was minimal αAlMnSi coarsening (increase in $\bar{r}$ from 54 ± 8 to 76 ± 11 nm - see Table II) between 5 h and 1000 h at 1000 °C. The somewhat more discrete αAlMnSi particles in AMS 63 after 2 h at 425 °C (Fig. 10a) coarsened more measurably, both within the αAl grains and at grain boundary junctions (Fig. 10b, c) giving a continuous increase in $\bar{r}$ from 34 ± 5 nm after 5 h to 83 ± 12 nm after 1000 h at 425 °C. Fig. 13a–c show $\bar{r}^3$ versus time t at 425 °C for αAlMnSi in the three materials. The associated slopes K and intercepts r_o^3 from Fig. 13a–c are given in Table III according to the equation [56, 57]

$$r^3 = r_o^3 + Kt \tag{3}$$

TABLE III Coarsening parameters K and r_o^3 (Equation 3) for αAlMnSi in melt spun AMS 135, 94 and 63 at 425 °C as given by Fig. 12a–c, along with corresponding results for 8009 sheet from [17]

System	AMS 63	AMS 94	AMS 135	8009 sheet
r_o^3, m^3	$1.1\,(\pm 0.4) \times 10^{-22}$	$2.6\,(\pm 0.6) \times 10^{-22}$	$3.5\,(\pm 0.9) \times 10^{-22}$	$5.8\,(\times 0.7) \times 10^{-23}$
K, m^3/s [17]	$1.4\,(\pm 0.6) \times 10^{-28}$	$5.8\,(\pm 2.9) \times 10^{-29}$	$2.8\,(\pm 1.5) \times 10^{-29}$	$1.2\,(\pm 0.5) \times 10^{-30}$

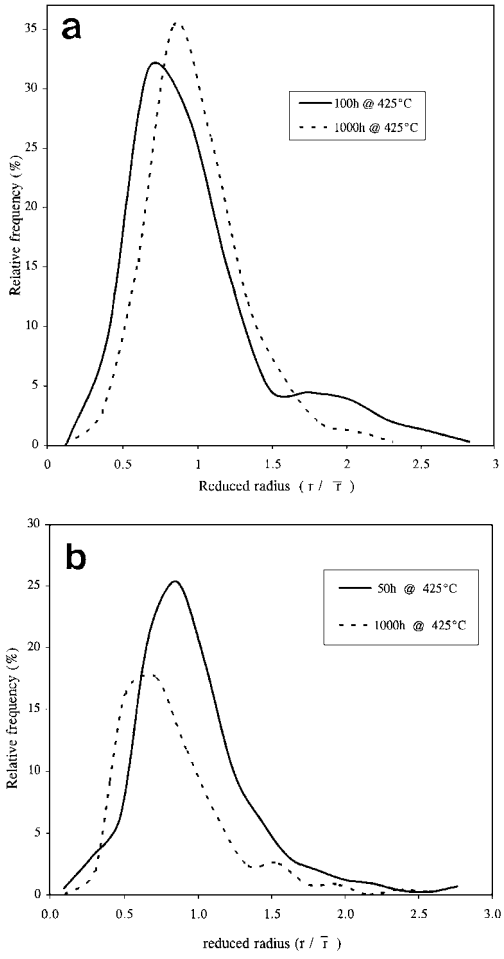

Figure 11 Showing silicide particle size distributions according to measurements from TEM micrographs for (a) AMS 135 after 100 and 1000 h at 425 °C (b) AMS 63 after 50 and 1000 h at 425 °C.

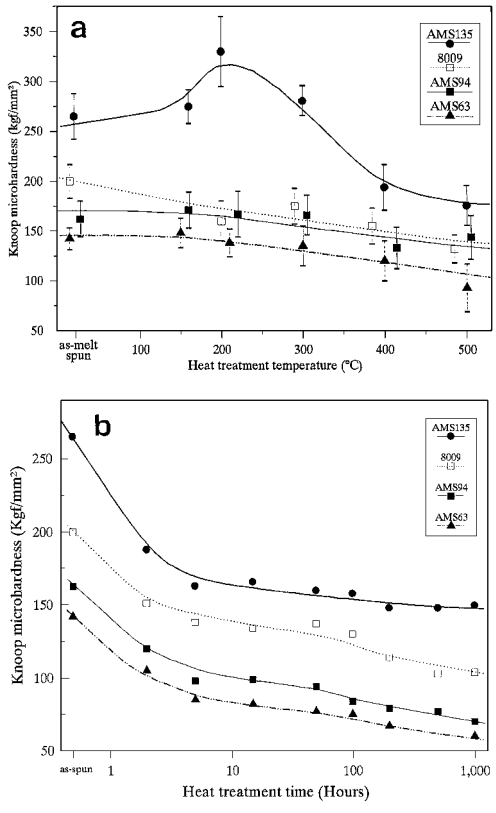

Figure 12 Knoop microhardness of AMS and 8009 ribbon versus (a) temperature of 2 h prior treatment up to 500 °C (b) duration of prior treatment at 425 °C.

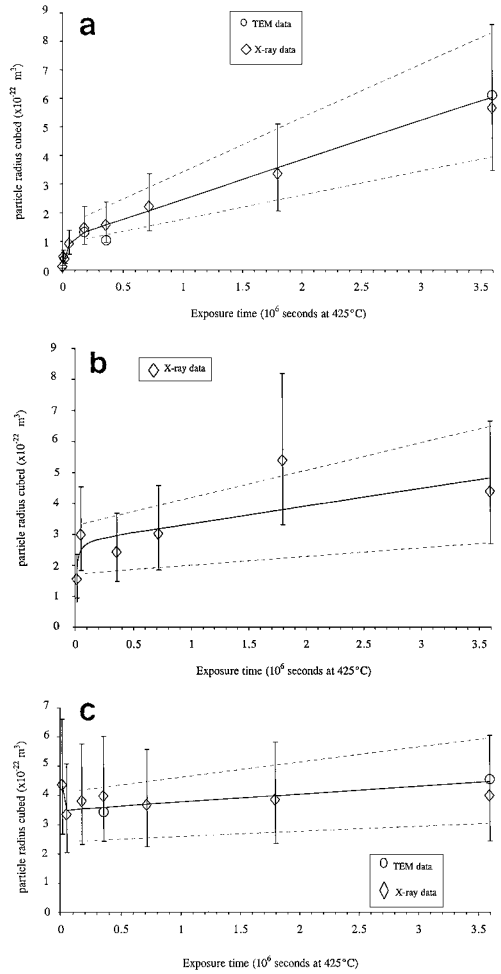

Figure 13 Cube of mean radius $\bar{r}$ of αAlMnSi versus time t at 425 °C for melt spun (a) AMS 63 (b) AMS 94 and (c) AMS 135, from data in Table II.

Our corresponding results for melt-spun 8009 alloy from [17] are included in Table III for comparison. The systematic decrease in K in proceeding from AMS 63 to 94 and 135 is evident along with a small increase in r_o^3. Both r_o^3 and K are considerably lower for $\alpha Al_{13}(Fe, V)_3Si$ in 8009 sheet. For low volume fractions of isolated particles in a matrix, coarsening isothermally under volume diffusion control, LSW theory [55, 56] predicts K in Equation 3 as $8DC_\infty V_m^2\gamma/9RT$ where D and C_∞ are solute diffusivity and equilibrium solid solubility at coarsening temperature T, V_m is molar volume of dispersoid, γ is interfacial energy and R is the gas constant. Results of [58–61] for diffusivity of Mn in Al are in excellent agreement giving $D = 2.0 \pm 0.4 \times 10^{-18}$ m^2/s at 425 °C while solubility data give $C_\infty = 0.1$ [62] or 0.07 [63] at % Mn $\equiv$ 100 or 70 mol/m^3. Taking $\gamma = 0.25$ J/m^2 as a representative value and $V_m = 6 \times 10^{-5}$ m^3/mol gives $K \sim 2.4 \times 10^{-29}$ m^3/s at 425 °C which is less by factors of 5 and 2 than the measured values for AMS 63 and 94 and in agreement with the measurements for AMS 135. The corresponding factor for $\alpha Al_{13}(Fe_1V)_3Si$ in 8009 sheet is 0.15*. The significance of this good level of

* An earlier version of this calculation [17] underestimated K by not taking account of the factor of 6 larger molecular volume of αAlMnSi (volume of unit cell per Mn atom) than the volume per atom in the αAl matrix.

agreement obtained between prediction and experiment is difficult to assess. The prediction assumes that Mn will control the rate of coarsening because it has lower diffusivity and solubility in the αAl matrix than Si, and any effects of Si on D and C_∞ for Mn in Al are negligible. No correction has been made for the effect of finite volume fraction f of the coarsening phase and the trend in Table III of a decrease in K with increase in f is the opposite of what is predicted [64]. As reported for other systems, the αAlMnSi particle size distributions (Fig. 11a, b) are skewed towards higher values of r, which is the opposite of what is predicted for steady state coarsening in the LSW model, and the distributions are wider than predicted. The prediction does not take into account the faster coarsening of particles situated on grain boundaries which was very evident for AMS 63. Perhaps the most notable feature of the results, however, is the remarkable stability of the chainlike configuration of linked αAlMnSi particles which characterize AMS 135 and 94 especially after extended treatment at 425 °C. The stability of $\alpha Al_{13}(Fe, V)_3Si$ in 8009 sheet at 425 °C is even greater, according to Table II, by a factor of 50 in K compared to melt spun AMS 94 which has a similar volume fraction of silicide to 8009. This increased resistance to coarsening of $\alpha Al_{13}(Fe, V)_3Si$ is partly attributable to the lower solubility in αAl of Fe compared with Mn but possibly also to a presumed effect of V in reducing the interfacial energy between the silicide and the αAl matrix. Another possible factor could be the finer initial particle size of the silicide in 8009 which would result in a smaller proportion of the silicide population being resident at grain boundaries, so that the average $\bar{r}$ was less affected by any accelerated coarsening on grain boundaries.

4.4. Mechanism of hardening as-spun and after heat treatment

The αAl cell size d ~50, ~100 and ~300 nm characteristic of AMS 135, 94 and 63 as-spun could give Hall-Petch contributions $k_y d^{-1/2}$ to hardening ~160, 110 and 80 kg/mm^2 based on k_y = 3.65 MPa mm$^{1/2}$ for αAl cells bounded by hard intermetallic [65] and assuming HK = $3\sigma_y$ for full plasticity under the indenter. Comparison with the experimental values of 260, 160 and 140 kg/mm^2 suggests additional contributions of 110, 50 and 60 kg/mm^2 from solid solution hardening in the αAl matrix. This proposed larger solid solution hardening contribution as-spun for AMS 135 is consistent with the evident age hardening response of this alloy in 2 h at 200 °C, further raising its hardness to 330 kg/mm^2, any such effect being much smaller for AMS 94 and 63.

A different model is appropriate for the microstructures evolved by 1000 h treatment at 425 °C which comprise chainlike or isolated αAlMnSi particles in a granular αAl matrix. The particles then harden by an Orowan mechanism giving a contribution [66]:

$$\Delta H = \frac{3MYGb(1-0.2\nu)^{1/2}}{2\pi(1-\nu)^{1/2}(\bar{L}-1.6\bar{r})} \ln\left(\frac{3.2\bar{r}}{b}\right) \quad (4)$$

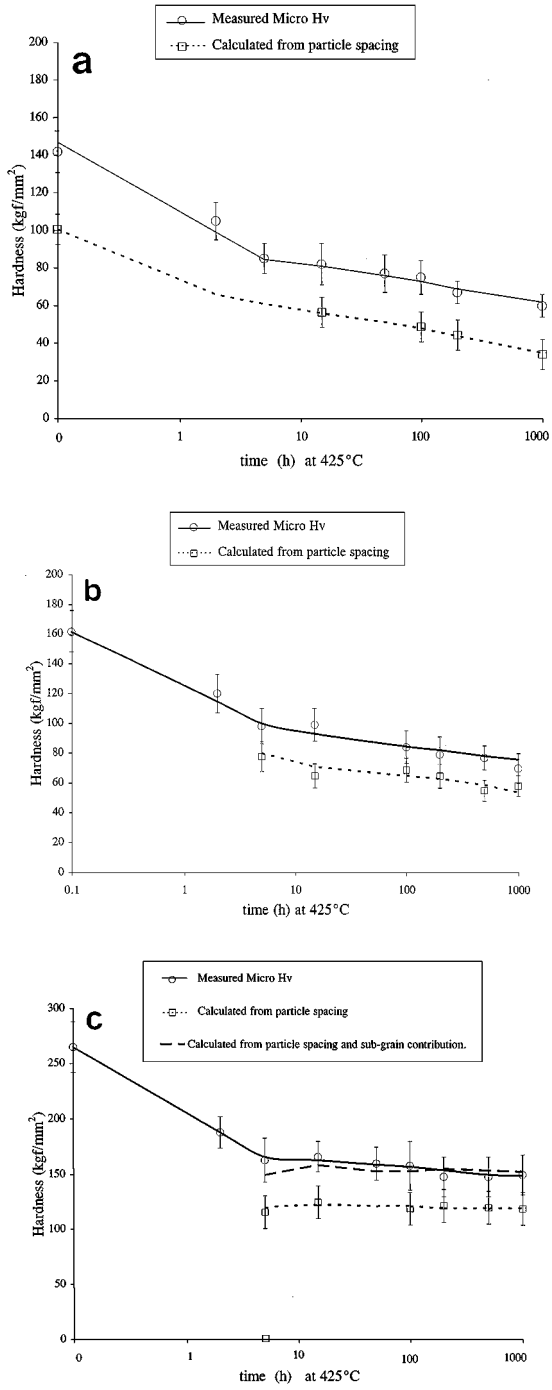

Figure 14 Measured hardness of AMS 63, 94 and 135 respectively versus time of prior treatment at 425 °C compared with predictions from Orowan hardening (Equation 4). For AMS 135 the effect of the additional contribution from Hall-Petch subgrain hardening is also shown.

where M is the Taylor factor (~3), Y ~ 0.9, G is shear modulus of the matrix (~26 GPa for Al), b is burgers vector (~0.286 nm), ν is Poisson's ratio (0.345 for Al), $\bar{L}$ is average centre to centre particle spacing and $\bar{r}$ is average particle radius. For a random distribution of spherical particles of uniform radius r, then $\bar{L}$ is given by 1.23r $(2\pi/3f)^{1/2}$ [67]. Equation 4 then predicts an Orowan contribution of 35 kg/mm^2 to the measured hardness 60 ± 6 kg/mm^2 of AMS 63 after 1000 h at 425 °C (using f = 0.17 and $\bar{r}$ = 85 nm from Tables I and II).

The remaining Hall-Petch contribution derives from the sub-grain size of ~600 nm of the αAl matrix, which

based on $k_y = 2.1\,MPa\,mm^{1/2}$ for pure aluminium [68], contributes 25 kg/mm^2. For AMS 135 after 1000 h at 425 °C, Equation 4 predicts $\Delta H = 105$ kg/mm^2 (using $f = 0.48$ and $\bar{r} = 77$ nm from Tables I and II), the residual Hall-Petch contribution amounting to 35 kg/mm^2 based on the αAl sub-grain size of 350 nm applicable, totaling up to 140 kg/mm^2, close to the measured value of 150 kg/mm^2. Fig. 14a–c compare the predicted Orowan contribution to measured hardness versus time at 425 °C for the three materials, the reduction in HK beyond 5 h for AMS 63 and 94 being entirely attributable to the decrease in Orowan contribution arising from the increase in $\bar{r}$ that results from αAlMnSi particle coarsening.

5. Conclusions

1. As melt spun AMS 135, 94 and 63, Al-Mn-Si alloys show an evolution of microstructure from primary icosahedral phase particles nucleating radial arrays of cellular αAl to less regular duplex arrays of αAl and αAlMnSi with decreasing alloying content and decreasing section thickness or reduced distance from the chill surface.

2. Heat treatment in the range 200 to 500 °C results in transformation of the icosahedral phase to equilibrium αAlMnSi where this is not already present, along with spheroidization and coarsening/coalescence of the αAlMnSi dispersoid to produce isolated spheroids in AMS 63 and very stable interlinked chains in AMS 135.

3. Mean silicide particle radius more than doubled between 2 and 1000 h at 425 °C for AMS 63 with a smaller measurable change for AMS 94 and virtually no measurable change for AMS 135.

4. The measured coarsening rate parameter of 1.4×10^{-28} m^3/s at 425 °C for AMS 63 was a factor of ten larger than predicted by the unmodified LSW theory, which does not take account of any contribution from accelerated coarsening of particles situated on αAl grain boundaries.

5. Hardness as-spun appears to be governed by a combination of Hall-Petch hardening from the αAl cell size and solid solution hardening of the αAl matrix, while evolution of hardness resulting from long term heat treatment at 425 °C could be effectively modeled by a combination of particle radius dependent Orowan hardening and αAl subgrain size dependent Hall-Petch hardening.

Acknowledgements

This work was carried out at the University of Sheffield with the support of DERA (Farnborough) under agreement 2031/145/RAE (F). The authors are grateful to British Aerospace at Warton for the supply of the 8009 sheet samples.

References

1. P. J. SKINNER, R. L. BYE, D. RAYBOULD and A. M. BROWN, *Scripta Met.* **20** (1986) 867.
2. P. GILMAN, *Metals and Materials* **6**(8) (1990) 504.
3. R. E. FRANK and J. A. HAWK, *Scripta Met.* **23** (1989) 113.
4. J. C. LEE, S. LEE, D. Y. LEE and N. J. KIM, *Met. Trans. A* **22A** (1991) 853; *Mater. Sci. Eng A* **A147** (1991) 33.
5. M. K. TSENG, X. F. CHEN, J. Q. WANG, X. ZE and B. J. ZHANG, *Mater. Sci. Eng. A* **A179**/**180** (1994) 412.
6. H. G. PARIS, F. R. BILLMAN, W. S. CEBULAK and J. I. PETIT, in "Rapid Solidification Processing: Principles and Technologies II," eds. R. Mehrabian et al., (Claitor's, Baton Rouge, LA, 1980) pp. 331–341.
7. G. TERLINDE, G. LÜTJERING, M. PETERS, J. C. WILLIAMS and H. G. PARIS, in "High Strength Materials for Aircraft," (DGM, Oberursel, 1982) pp. 95–112.
8. T. AHRENS, A. GYSLER and G. LÜTJERING, *Z Metallkunde*. **76** (1985) 391.
9. G. TERLINDE, M. PETERS, G. LÜTJERING and J. C. WILLIAMS, *ibid* **78** (1987) 607.
10. J. A. HAWK, L. M. ANGERS and H. G. F. WILSDORF, in "Dispersion Strengthened Aluminium Alloys," eds. Y. W. Kim and W. M. Griffith, (MMMS, Warrendale, Pa, 1988) pp. 337–354.
11. B. SAAL, J. ALBRECHT, G. LÜTJERING, J. BECKER and G. FISCHER, in "Light Weight Alloys for Aerospace Applications," eds. E. W. Lee et al., (TMS, Warrendale, Pa, 1989) p. 3.
12. G. LÜTJERING, B. SOPART and J. ALBRECHT, in "Science and Engineering of Light Metals," eds. K. Hirano et al., (The Japanese Institute of Light Metals, Tokyo, 1991) pp. 27–34.
13. O. RODER, J. ALBRECHT and G. LÜTJERING, *Proc. Euro Mat. 94*, ed. B. Vorsatz and E. Szöke, vol II pp. 641–652.
14. H. G. F. WILSDORF, L. M. ANGERS, J. K. BRIGGS and J. A. HAWK, *Advances in P/M* **3** (1989) 269.
15. J. A. HAWK, J. K. BRIGGS and H. G. F. WILSDORF, *ibid*. 301.
16. H. G. F. WILSDORF, J. K. BRIGGS and L. M. ANGERS, *Key Engineering Materials* **38/39** (1990) 299.
17. D. M. J. WILKES, H. JONES and R. W. GARDINER, *Mater. Sci. Forum*. **217-222** (1996) 943.
18. R. HAMBLETON, H. JONES and W. M. RAINFORTH, *Mater. Sci. Eng.* **A226/8** (1997) 157.
19. M. COOPER and K. ROBINSON, *Acta Cryst.* **20** (1966) 614.
20. P. A. BANCEL, P. A. HEINEY, P. W. STEPHENS, A. I. GOLDMAN and P. M. HORN, *Phys. Rev. Lett.* **54** (1985) 2422.
21. J. W. CAHN, D. SHECHTMAN and D. GRATIAS, *J. Mater. Res.* **1** (1986) 13.
22. A. INOUE, H. M. KIMURA, T. MASUMOTO, A. P. TSAI and Y. BIZEN, *J. Mater. Sci. Lett.* **6** (1987) 771.
23. H. JONES, *Mater. Sci. Eng.* **5** (1969) 1.
24. W. J. BOETTINGER, L. BENDERSKY and J. G. EARLY, *Met. Trans. A* **17A** (1986) 781.
25. M. CHU and D. A. GRANGER, *Met. Trans. A* **21A** (1990) 205.
26. R. J. SCHAEFER, L. A. BENDERSKY, D. SHECHTMAN, W. J. BOETTINGER and F. S. BIANCANIELLO, *Met. Trans. A* **17A** (1986) 2117.
27. M. X. QUAN and B. C. GIESSEN, *Mater. Res. Soc. Proc.* **58** (1986) 241.
28. K. F. KOBAYASHI, H. KAWAURA and P. H. SHINGU, in 'Aluminium Alloys: Their Physical and Mechanical Properties,' eds. E. A. Starke and T. H. Sanders, *EMAS* **1** (1986) 247.
29. M. HARMELIN, in "Quasicrystalline Materials," eds. C. H. Janot and J. M. Dubois, (World Scientific, 1988) pp. 19–28.
30. C. BERGER, F. CYROT-LACHMANN, J. DEVENYI, G. FOURCAUDOT, P. GERMI, J. C. GRIECO and D. PAVUNA, *J. Phys. Cond. Matt.* **1** (1989) 3421.
31. Y. ZHANG, T. YAMANE, S. SAJI and T. TAKAHASHI, *J. Mater. Sci.* **28** (1993) 3235.
32. L. A. BENDERSKY and S. D. RIDDER, *J. Mater. Res.* **1** (1986) 405.
33. H. JONES, *Materials Letters* **26** (1996) 133.
34. H. JONES, *Mater. Sci. Eng.* **65** (1984) 145.
35. D. SHECHTMAN, I. BLECH, D. GRATIAS and J. W. CAHN, *Phys. Rev. Lett.* **53** (1984) 1951.
36. R. A. DUNLAP and K. DINI, *Canad. J. Phys.* **63** (1985) 1267.
37. F. H. SAMUEL, A. M. SAMUEL, A. de JONCKERE and F. GERIN, *Met. Trans. A* **17A** (1986) 1671.
38. R. LÜCK, H. HAAS, F. SOMMER and B. PREDEL, *Scripta Met.* **20** (1986) 677.
39. G. REDDY, J. A. SEKHAR and P. V. RAO, *Scripta Met.* **21** (1987) 13.

40. K. F. KELTON and J. C. HOLZER, *Phys. Rev. B* **37** (1988) 3940.
41. U. KÖSTER and B. SCHUMACHER, *Mater. Sci. Eng.* **99** (1988) 417.
42. K. Y. ZHANG and N. YU, *Scripta Met.* **23** (1989) 1123.
43. D. H. KIM, K. CHATTOPADHYAY and B. CANTOR, *Phil. Mag. A* **62** (1990) 157.
44. Y. YAN, R. WANG and J. GUI, *J. Phys. Cond. Matt.* **2** (1990) 7733.
45. K. K. FUNG and Y. Q. ZHAN, *Phil. Mag. B* **54** (1986) L27.
46. J. PANNETIER, J. M. DUBOIS, C. JANOT and C. BILDE, *Phil. Mag. B* **55** (1987) 435.
47. D. BAXTER, R. SCHULTZ, G. J. C. CARPENTER and J. D. STROM-OLSEN, *Mater. Sci. Eng.* **99** (1988) 99.
48. T. OHASHI, N. FUKATSU and K. ASAI, *J. Mater. Sci.* **24** (1989) 3717.
49. V. SRINIVAS and R. A. DUNLAP, *Mater. Sci. Eng. A* **A125** (1990) 115.
50. V. HANSEN, B. ANDERSON, J. E. TIBBALLS and J. GJØNNES, *Met. Mater. Trans. B* **26B** (1995) 839.
51. V. HANSEN and J. GJØNNES, *Phil. Mag. A* **73** (1996) 1147.
52. A. K. SRIVASTAVA and S. RANGANATHAN, *Acta Mater.* **44** (1996) 2935.
53. V. ELSER and C. L. HENLEY, *Phys. Rev. Lett.* **55** (1985) 2883.
54. P. DONNADIEU, G. LAPASSET and T. H. SANDERS, *Phil. Mag. Lett.* **70** (1994) 319.
55. W. J. PARK, E. R. BAEK, S. LEE and N. J. KIM, in "Lightweight Alloys for Aerospace Applications II," eds., E. W. Lee and N. J. Kim (TMS, Warrendale, Pa, 1991) pp. 219–229.
56. L. M. LIFSHITZ and V. V. SLYOZOV, *J. Phys. Chem. Solids* **19** (1961) 35.
57. C. WAGNER, *Z. Electrochem* **65** (1961) 581.
58. G. M. HOOD and R. J. SCHULTZE, *Phil Mag.* **23** (1971) 1479.
59. S. FUJIKAWA and K. HIRANO, *Mater. Sci. Forum.* **13/14** (1987) 539.
60. Y. MINAMO, T. YAMANE, S. NAKAGAWA, H. ARAKI and K. I. HIRANO, *J. Jap. Inst. Light Metals* **37** (1987) 72.
61. G. RUMMEL, T. ZUMKLEY, M. EGGERSMANN, K. FREITAG and H. MEHRER, *Z. Metallkunde* **85** (1995) 122.
62. L. F. MONDOLFO, "Aluminium Alloys: Structure and Properties," (Butterworths, 1976).
63. A. J. McALISTER and J. L. MURRAY, *Bull. Alloy Phase Diagrams* **8** (1987) 438–447.
64. A. J. ARDELL, in "Phase Transformations '87," ed. G. W. Lorimer, (Institute of Metals, 1988) pp 485–494.
65. H. NAGAHAMA, K. OHTERA, K. HIGASHI, A. INOUE and T. MASUMOTO, *Phil. Mag. Lett.* **67** (1993) 225.
66. E. NEMBACH, "Particle Strengthening of Metals and Alloys," (Wiley, New York, 1997) 6.1.2.
67. M. F. ASHBY, *Z. Metallkunde* **55** (1964) 5.
68. T. YAMANE, Y. MASUGUTA and K. HIRAO, *J. Jap. Inst. Met.* **36** (1986) 319.

Received 1 April
and accepted 12 August 1998